Mechanical and microstructural analysis on hydrogen-related fracture in a martensitic steel

Akinobu Shibata, Yazid Madi, Kazuho Okada, Nobuhiro Tsuji, Jacques Besson

Mechanical and microstructural analysis on hydrogen-related fracture in a martensitic steel

Akinobu Shibata[1,2,3*], Yazid Madi[3], Kazuho Okada[1], Nobuhiro Tsuji[1,2], Jacques Besson[3]

[1] Department of Materials Science and Engineering, Kyoto University, Yoshida-honmachi, Sakyo-ku, Kyoto 606-8501, Japan

[2] Elements Strategy Initiative for Structural Materials (ESISM), Kyoto University, Yoshida-honmachi, Sakyo-ku, Kyoto 606-8501, Japan

[3] Centre des Matériaux, MINES ParisTech, CNRS UMR 7633, BP 87, 91003, Evry, France

[*] Corresponding author Tel: +81-75-753-5468, Fax: +81-75-753-4978

E-mail: shibata.akinobu.5x@kyoto-u.ac.jp

Abstract:

The present study quantitatively evaluated mechanical response of hydrogen-related fracture in the as-quenched martensitic steel and correlated it to crack propagation behavior analyzed by microstructure observations. The crack-growth resistance curves revealed that the hydrogen-related intergranular cracks propagated in a stable manner even when the diffusible hydrogen content was large. Fracture initiation toughness was decreased significantly by small amounts of diffusible hydrogen. With further increasing diffusible hydrogen content, however, the fracture initiation toughness did not change and remained almost constant. On the other hand, tearing modulus, corresponding to crack-growth resistance, decreased rather gradually with increasing diffusible hydrogen content. The microstructure observations confirmed that the hydrogen-related crack propagated discontinuously in a stepwise manner on a microscopic scale. Accordingly, it was proposed that the microscopic discontinuous crack propagation could be the possible reason for the stable crack propagation.

Keywords: Hydrogen embrittlement; Martensitic steel; Fracture mechanisms; Crack growth resistance curve; Electron backscattering diffraction

1. Introduction

Hydrogen induces premature fracture in metals and alloys, so-called hydrogen embrittlement, hydrogen-related fracture or delayed fracture. Several models have been proposed to account for hydrogen-related fracture, such as high hydrogen pressure bubble or void [1], hydrogen-induced reduction in surface energy [2, 3], hydrogen-enhanced dislocation ejection from the surface or near surface region [4], hydrogen-induced reduction in cohesive energy [5-7], hydrogen-enhanced localized plasticity [8-11], hydrogen-assisted vacancy production [12, 13]. Each model of hydrogen embrittlement was reviewed in detail by Robertson et al. [14]. Nowadays, it has been recognized that no single model mentioned above can comprehensively account for all the phenomena associated with hydrogen embrittlement. Rather, in many cases, a combination of different models is reasonable to understand hydrogen-related fracture behavior.

It is well known that susceptibility to hydrogen embrittlement increases with increasing strength of material. In other words, high strength steels are highly sensitive to hydrogen embrittlement. Because a certain amount of hydrogen is inevitably introduced into steel products during fabrication process or from environment, hydrogen embrittlement is now becoming one of the major concerns in steel society. A lath martensite structure, which often appears in most high strength steels, exhibits a complicated microstructure consisting of several structural units with different length scale: lath, block, packet and prior austenite grain [15, 16]. For aiming to suppress hydrogen embrittlement of high strength martensitic steels through microstructure control, many efforts have been conducted to

understand relationship between the complicated microstructure of martensite and hydrogen-related fracture behavior. In general, two typical fracture modes occur for hydrogen-related fracture in steels: quasi-cleavage fracture and intergranular fracture. Kim et al. [17, 18] and Nagao et al. [19] reported that the hydrogen-related quasi-cleavage fracture surfaces were parallel to the lath boundaries. On the other hand, Shibata et al. [20-23] insisted through precise crystallographic orientation analysis that the hydrogen-related quasi-cleavage fracture propagated parallel to {011} planes within lath. For the hydrogen-related intergranular fracture, many studies proposed that the cracks propagated on prior austenite grain boundaries [24-29].

For developing advanced high strength steels with high resistance to hydrogen embrittlement from theoretical background, in addition to microstructural analysis, we consider that it is very important to accurately understand the mechanical response of hydrogen embrittled steels and correlate it to crack propagation behavior. In general, fracture process can be divided into three stages on a microscopic view: (i) crack initiation, (ii) start of crack propagation and (iii) stable / unstable crack propagation to whole specimen (or material) leading to final rupture. Presently, many of the previous works have evaluated hydrogen embrittlement properties by a simple uniaxial tensile test using smooth specimens. However, the obtained tensile properties, such as fracture stress or tensile ductility, can be used only as a relative indicator of susceptibility to hydrogen embrittlement. In addition, it is nearly impossible to break the obtained tensile properties down into the mechanical response of each microscopic fracture stage. On the other hand, it is well known that a crack-growth resistance curve obtained by

elastic – plastic fracture mechanics experiments is useful to evaluate fracture toughness properties corresponding to microscopic fracture stages. The resistance curve technique has been frequently applied to study micromechanism of ductile fracture [30]. This technique was recently also applied in several studies to understand hydrogen-related fracture behavior [31-41]. For example, Nagumo et al. [31] obtained crack-growth resistance curves of ferrite – pearlite steels by three-point bending tests and confirmed that the crack-growth resistance was decreased by the presence of hydrogen. They also discussed the reduction of crack-growth resistance from the viewpoint of hydrogen-enhanced void nucleation. Moreover, Somerday et al. [33, 34, 36-38] studied effect of hydrogen on crack initiation and crack growth behaviors in several austenitic stainless steels and Cr-Mo / Ni-Cr-Mo low-alloy pressure vessel steels based on the experimentally measured crack-growth resistance curves.

The present study utilized the crack-growth resistance curve technique for understanding hydrogen-related fracture behavior of a high strength martensitic steel. Tests using the unloading compliance technique were conducted to obtain crack-growth resistance curves ($J - \Delta a$ resistance curves) and evaluate effect of electrochemically introduced hydrogen on fracture initiation toughness and tearing modulus. The fracture initiation toughness is related to the microscopic fracture stages (i) and (ii). On the other hand, the tearing modulus represents crack-growth resistance corresponding to the microscopic fracture stage (iii). Tensile tests on smooth and notched axisymmetric tensile bars were also carried out to evaluate macroscopic fracture stresses. In addition, we carefully investigated

crack propagation behavior through microstructure observations and discussed the correlation between fracture toughness properties and crack propagation behavior.

2. Experimental Procedure

An as-quenched low-carbon martensitic steel (8Ni-0.1C steel) was selected in the present study, because special attentions to type, morphology and size distribution of carbides were not necessary. Moreover, block and packet sizes of low-carbon martensitic steels are relatively large [42] so that we can effectively study the relationship between microstructure and crack propagation behavior by using the as-quenched low carbon martensitic steel. The detailed chemical composition (wt. %) of the steel is C: 0.116, Si: 0.005, Mn: 0.01, P: 0.001, S: 0.0015, Al: 0.033, Ni: 7.94, Fe: bal. Homogenized steel plates with a thickness of 15 mm were austenitized at 1000 °C for 30 min followed by ice-brine quenching and sub-zero cooling in liquid nitrogen. As shown in the optical microscopy image of **Figure 1**, the heat-treated specimen exhibited a fully lath martensite structure. Smooth tensile bar (ST) specimens, notched tensile bar (NT) specimens with a notch radius (R) of 2.4 mm and compact tension (CT) specimens were cut from the heat-treated plates. All the tensile bar specimens have a minimum diameter equal to 6 mm. The CT specimens with a thickness (B) of 12.5 mm and a width (W) of 25 mm were fatigue pre-cracked in order to obtain an initial crack length of approximately 12.5 mm (0.5W), according to ASTM E1820. Then, side grooves were introduced into the pre-cracked CT specimens so that the thickness at the roots of the side grooves (B_N) was 10 mm. **Figure 2** shows

schematic illustrations of the ST, NT and CT specimens.

The ST, NT and CT specimens were cathodically pre-charged with hydrogen in an aqueous solution of 3 % NaCl + 3 g L^{-1} NH_4SCN for 259.2 ks (3 days). A platinum wire was used as a counter electrode. Our preliminary experiments suggested that charging period of 3 days was necessary to make hydrogen homogenously distributed inside the present specimen geometries. The current density of the hydrogen charging was changed ranging from 0.625 A m^{-2} to 3 A m^{-2} to obtain the specimens with different hydrogen contents. Only after hydrogen charging at a current density of 3 A m^{-2}, tiny and shallow surface cracks were rarely visible on the specimen surface. However, we could not find that the surface cracks propagated during the mechanical tests. **Figure 3** presents diffusible hydrogen content (H_D) of the specimens for different hydrogen charging conditions measured by thermal desorption spectrometry (TDS) analysis. For the TDS analysis, specimens with a dimension of ~ 12.5 × 15 × 15 mm^3 were used. Here, the H_D was defined as the cumulative hydrogen content desorbed below 400 °C, where the first TDS peak ended. Based on the previous papers [26, 43], we can consider that the diffusible hydrogen, which was desorbed below 400 °C, involved hydrogen trapped at lattice defects (dislocation, grain boundary, and so on) as well as hydrogen at interstitial lattice sites. As shown in **Figure 3**, we obtained the hydrogen-charged specimens with H_D of 0.28 wt. ppm (0.625 A m^{-2}), 0.42 wt. ppm (1.25 A m^{-2}), 1.01 wt. ppm (2 A m^{-2}) and 4.00 wt. ppm (3 A m^{-2}). It should be noted that diffusible hydrogen was not detected in the TDS analysis for the uncharged specimen. The TDS measurements and the mechanical tests (slow strain rate tensile tests and

unloading compliance tests described below) were always started 2.4 ks after completion of the hydrogen charging.

Slow strain rate tensile tests at an initial strain rate ($\dot{\varepsilon}$) of 8.3×10^{-6} s^{-1} were conducted for the ST and NT specimens. An extensometer with a gauge length of 27 mm was used to measure displacement and the test was controlled by the extensometer. Displacement rate ($\dot{L}$) of the tensile test for the NT specimen was determined so as to approximately obtain the same strain rate in the notch area as: $2 \times R \times \dot{\varepsilon}$ (this simple rule can be checked using finite element simulations assuming an elasto-plastic behavior). From the slow strain rate tensile tests, we obtained nominal stress – nominal strain curves. The nominal stress is F / S_0, where F is the applied force and S_0 is the initial cross section area. The nominal strain for the ST specimen is ΔL / L_0 and that for the NT specimen is ΔL / ($2 \times R$). The L_0 and ΔL are the initial gauge length and the gauge length increase, respectively.

Crack growth behavior was investigated using the CT specimen. Unloading compliance tests based on the single specimen test method were performed to obtain J – Δa resistance curves in accordance with ASTM E1820. J is the J-integral value and Δa is the crack extension length. Crack mouth opening displacement during the unloading compliance test was measured by clip gauge. The elastic compliance at a certain displacement was determined from unload / reload sequences repeated three times. Each of the unload / reload sequences was conducted for a displacement interval of 0.025 mm and the crack extension length at each stage was calculated from the elastic compliance according to ASTM E1820. J was computed from $J = J_{el} + J_{pl}$, where J_{el} was computed from linear elastic

fracture mechanics and J_{pl} was incrementally computed using the plastic area under the load – displacement curve (ASTM E1820). The unloading compliance tests (except for unload / reload sequences) were carried out under displacement control. It is difficult to evaluate actual strain rate at crack tip of the CT specimen during the unloading compliance test. In order to make strain rate sufficiently slow, the rate of crack mouth opening displacement for the unloading compliance test was chosen as 2.5×10^{-5} mm s^{-1}. The corresponding initial rate of stress intensity factor ($\dot{K}$) for $a / W =$ 0.5 was 8.5×10^{-3} MPa $m^{1/2}$ s^{-1}. In order to ensure reproducibility of crack growth behavior, the unloading compliance test for each charging condition was repeated three times.

Fracture surfaces of the tested ST, NT and CT specimens were observed using scanning electron microscopy (SEM, LEO: 1450VP, JEOL: JSM-7100F and JEOL: JSM-7800F). To study crack growth behavior from a microstructural point of view, crystal orientation mappings at the mid-thickness sections of the tested CT specimens were performed by electron backscattering diffraction (EBSD) with a step size of 0.1 μm using SEM operated at 15 kV. The specimen surfaces for EBSD measurement were prepared by vibration polishing with a 0.02 μm colloidal silica suspension. The EBSD measurement and analysis were performed with the TSL OIM Data Collection program and the TSL OIM Analysis program, respectively.

3. Results

3.1 Uniaxial tensile test results using ST and NT specimens

Figures 4 (a, b) show nominal stress – nominal strain curves of the ST specimens (a) and the NT specimens (b) with different H_D, respectively. The uncharged ST specimen exhibited large nominal elongation up to about 10 %. The hydrogen-charged ST specimen with H_D of 0.28 wt. ppm exhibited some plasticity before fracture. In contrast, the hydrogen-charged ST specimens with H_D more than 0.42 wt. ppm fractured within the elastic strain regime. The elongation of the uncharged NT specimen was limited compared to the uncharged ST specimen. In addition, the hydrogen-charged NT specimens did not exhibit macroscopic plastic deformation before fracture. The macroscopic fracture stresses (nominal stresses) of ST and NT specimens are summarized in **Figure 4 (c)** as a function of H_D. In the case of the uncharged ST specimen, the maximum nominal flow stress (tensile strength) was plotted. For both the ST and NT specimens, the macroscopic fracture stresses decreased suddenly with small values of H_D around 0.5 wt. ppm and then became constant with further increasing H_D. The saturation of hydrogen degradation at higher hydrogen content was also reported in various steels [26, 44, 45].

Secondary electron (SE) images using SEM (SEM / SE images) of **Figure 5** show fracture surfaces of (a) the uncharged ST specimen, (b) the uncharged NT specimen, (c) the hydrogen-charged ST specimen (H_D = 4.00 wt. ppm), and (d) the hydrogen-charged NT specimen (H_D = 4.00 wt. ppm). A fully ductile surface with dimples is observed in the uncharged ST specimen. On the other hand, the fracture surface of the uncharged NT specimen consists of intergranular surfaces. This is consistent with the stress – strain curve of the uncharged NT specimen in **Figure 4 (b)**, where the uncharged NT

specimen had limited elongation. This is the characteristic of the used martensitic steel, that is, even in the uncharged state, large stress concentration at notch root induced brittle intergranular fracture. Almost all the areas of the fracture surfaces in the hydrogen-charged ST and NT specimens are covered with intergranular surfaces, though some dimples and quasi-cleavage facets with serrated markings can be observed. The positions of typical dimples and quasi-cleavage facets are indicated by white arrows, and **Figures 5 (e, f)** show high magnification SEM / SE images of the quasi-cleavage facets observed in the hydrogen-charged ST and NT specimens (H_D = 4.00 wt. ppm). We also confirmed that fracture surfaces of the other hydrogen-charged ST and NT specimens (H_D = 0.28 ~ 1.01 wt. ppm) were quite similar to those of **Figures 5 (c, d)** with intergranular surfaces and small amounts of dimples / quasi-cleavage facets. Accordingly, we can conclude that the major mode of hydrogen-related fractures in both the ST and NT specimens was intergranular.

3.2 Unloading compliance test results using CT specimens

Load – crack mouth opening displacement curves of the CT specimens with different H_D are presented in **Figure 6 (a)**. We can confirm that the maximum load decreased with increasing H_D. It can be seen that the slopes of unload / reload sequence decreased during the unloading compliance tests. By analyzing the crack extension length (Δa) from the change in compliance during the test according to ASTM E1820, we obtained J – Δa resistance curves. The representative J – Δa resistance curves for each hydrogen-charged specimen are shown in **Figure 6 (b)**. In order to confirm

the reliability of crack extension length evaluated by the unloading compliance technique, crack extension length was also measured using fracture surface image of one uncharged CT specimen. After the unloading compliance test, the specimen was thermally etched at 300 °C for 30 min in air, and then fractured in liquid nitrogen. The size of thermally etched region, corresponding to the crack extension length after completion of the unloading compliance test, was measured at nine equally spaced points on the fracture surface image according to ASTM E1820. The difference between the crack extension length evaluated by the unloading compliance technique and that using fracture surface image was 0.11 mm, indicating that the present unloading compliance technique can evaluate crack extension length.

As shown in **Figure 6 (b)**, the $J - \Delta a$ resistance curves of the uncharged CT specimen and the hydrogen-charged CT specimen with H_D of 0.28 wt. ppm were similar. For the hydrogen-charged CT specimens with H_D more than 0.42 wt. ppm, cracks started to propagate at significantly low J-integral values compared with the uncharged CT specimen. However, a positive slope on the $J - \Delta a$ resistance curves can be observed even after the start of crack propagation. This indicates that the hydrogen-related fracture was not completely unstable premature fracture, but the crack propagated in a stable manner to some extent even when H_D was large. The work by Kameda and McMahon [46] also suggested that stable crack propagation could happen in hydrogen-related fracture of the high strength martensitic steel. Here, we simply defines stable crack growth as the one which requires increment of J-integral for further growth (i.e., $dJ / d\Delta a > 0$). Chan [47] considered crack growth

with finite and positive $dJ / d\Delta a$ as a stable crack growth because strain energy should be supplied by external load for further crack extension. Instability can also correspond to the case where to a decrease of the force is triggered for an infinitesimal variation of the applied displacement. This situation is avoided provided $dJ / d\Delta a$ is large enough and the machine stiffness is high [48]. This situation was never encountered during testing.

From the $J - \Delta a$ resistance curves shown in **Figure 6 (b)**, we evaluated fracture initiation toughness (J_{IC}) and dimensionless tearing modulus (T_R). The fracture initiation toughness was defined as the J-integral value at the intersection of the 0.2 mm offset line with the $J - \Delta a$ resistance curve. According to ASTM E1820, the slope of 0.2 mm offset line is $2 \times \sigma_Y$, where σ_Y is the average of 0.2 % offset yield strength and ultimate tensile strength. Because the hydrogen-charged specimens fractured within the elastic strain regime, we used σ_Y of 1055 MPa which was derived from the stress – strain curve of the uncharged ST specimen. We confirmed that all the uncharged and hydrogen-charged CT specimens satisfied the specimen size criteria for obtaining valid plane-strain J_{IC} according to ASTM E1820. The tearing modulus, which corresponds to crack-growth resistance, was derived from the following equation;

$$T_R = \frac{E}{\sigma_0^2}\frac{dJ}{d\Delta a} \quad (1)$$

where E is a Young modulus (= 200GPa), σ_0 is a 0.2% offset yield strength and $dJ / d\Delta a$ is an average slope of the linear region after intersection of the 0.2 mm offset line in the $J - \Delta a$ resistance curve. Chan [47] proposed that T_R could be used as a parameter of crack-growth resistance even when the

fracture mode was brittle. Because σ_0 of the hydrogen-charged specimens could not be evaluated from the stress – strain curves of Figure 4(a), we used σ_0 of the uncharged ST specimen (920 MPa) assuming that σ_0 does not depend on H_D very much. Changes in fracture initiation toughness and tearing modulus with H_D are presented in **Figures 7 (a, b)**, respectively. As shown in **Figure 7 (a)**, the fracture initiation toughness decreased significantly for relatively small values of H_D, around 0.5 wt. ppm. With further increasing H_D, however, the fracture initiation toughness did not change and remained almost constant. As the fracture initiation toughness can be considered to be the toughness property corresponding to the onset of crack propagation, we found that the hydrogen-related crack easily started to propagate for small values of H_D. On the other hand, the tearing modulus decreased rather gradually with increasing H_D (**Figure 7 (b)**).

3.3 SEM and EBSD analysis for the tested-CT specimens

SEM / SE images showing fracture surfaces of the CT specimens are shown in **Figure 8**. Left sides correspond to the fatigue pre-cracks and the cracks propagated from left to right sides in the SEM / SE images. As in the case of the tensile-tested NT specimens (**Figure 5 (b, d)**), the fracture surfaces of both the uncharged and hydrogen-charged CT specimens comprise mainly intergranular surfaces and small amounts of dimples / quasi-cleavage facets. The positions of typical dimples and quasi-cleavage facets are indicated by white arrows.

In order to investigate macroscopic crack propagation behavior, the mid-thickness sections of the

tested-CT specimens were observed by SEM / SE as shown in **Figure 9**. As in the case with **Figure 8**, the cracks propagated from left to right sides in the SEM / SE images. It is clear that the macroscopic crack morphologies are different depending on H_D. For the uncharged CT specimen (**Figure 9 (a)**) and the hydrogen-charged CT specimen with small H_D (H_D = 0.28 wt. ppm) (**Figure 9 (b)**), many un-cracked ligaments can be observed as indicated by white arrows. The existence of many un-cracked ligaments suggests that discontinuous crack propagation occurred. As shown in **Figures 9 (c) – (e)**, on the other hand, the cracks propagated rather continuously for the hydrogen-charged CT specimens with H_D more than 0.42 wt. ppm. Therefore we can conclude that macroscopic crack propagation tended to be more continuous with increasing H_D.

Figure 10 (a) shows a back-scattering electron (BSE) image using SEM (SEM / BSE image) around an area about 150 μm ahead of the main crack in the uncharged CT specimen. Micro-cracks are visible in the SEM / BSE image. An EBSD orientation map corresponding to **Figure 10 (a)** is presented in **Figure 10 (b)**. The colors in the EBSD orientation map express the orientations parallel to the normal direction (ND) of the observed section and the stereographic triangle inserted in the EBSD orientation map shows the correspondence between color and crystal orientation along ND. Additionally, the positions of micro-cracks and prior austenite grain boundaries determined by orientation analysis are indicated by black solid lines and white broken lines, respectively. Although there are various kinds of high angle boundaries in lath martensite structure, such as block boundary, packet boundary and prior austenite grain boundary, we can find that the micro-cracks apparently

propagated along the prior austenite grain boundaries. This is consistent with SEM / SE image of **Figure 8 (a)** where the fracture surface comprised mainly intergranular surfaces. **Figures 10 (c, d)** show a high magnification SEM / BSE image and an EBSD orientation map whose observed area correspond to the white rectangle in (a). We can confirm that, even on a microscopic scale, the micro-crack propagated on the prior austenite grain boundary.

An SEM / BSE image and an EBSD orientation map of an area about 100 μm ahead of the main crack in the hydrogen-charged CT specimen (H_D = 4.00 wt. ppm) are shown in **Figures 11 (a, b)**. The black and white broken lines represent the positions of micro-cracks and prior austenite grain boundaries, respectively. As well as the case of the uncharged CT specimen, the hydrogen-related micro-cracks apparently propagated along the prior austenite grain boundaries. However, the high magnification SEM / BSE image and the EBSD orientation map of **Figures 11 (c, d)** revealed that the small un-cracked ligaments existed on the prior austenite grain boundary (yellow arrows). Moreover, the micro-crack partly deviated from the prior austenite grain boundary at the position indicated by red arrow. Hydrogen-related crack propagations not exactly on but in the vicinity of prior austenite grain boundaries have been reported previously [20-22]. We confirmed the similar tendency in the other hydrogen-charged CT specimens (H_D = 0.42 ~ 1.01 wt. ppm). Based on the observation results, we found that the hydrogen-related micro-cracks propagated discontinuously in a stepwise manner on a microscopic scale, although the cracks were rather continuous macroscopically.

4. Discussion

Hydrogen can move even at room temperature due to its high diffusivity. It is a common understanding that hydrogen diffusion / accumulation during deformation has an important influence on hydrogen-related fracture. Previous studies proposed that prior austenite grain boundary was a major trapping site of hydrogen in lath martensite structure [49, 50]. We also reported using hydrogen microprint technique that hydrogen tended to accumulate around prior austenite grain boundaries during tensile deformation at a slow strain rate ($\dot{\varepsilon} = 8.3 \times 10^{-6}$ s^{-1}), but no hydrogen accumulation at prior austenite grain boundaries was confirmed when the strain rate was fast ($\dot{\varepsilon} = 8.3 \times 10^{-1}$ s^{-1}) [51]. One can imagine that there was a large residual stress around the tip of fatigue pre-crack in the CT specimen that was introduced during the fatigue pre-cracking process. Many papers proposed that hydrogen tended to accumulate in the region with high stress field, particularly high hydrostatic tensile stress, and large plastic strain [52-55]. Assuming that hydrogen accumulated at prior austenite grain boundaries in the vicinity of the tip of fatigue pre-crack during the hydrogen pre-charging process, the cracks easily formed and started to propagate during the fracture mechanics test (unloading compliance test) even when the global H_D was small. This would lead to the rapid decrease of fracture initiation toughness with small H_D. On the other hand, there was no specific site with high hydrostatic tensile stress or large plastic strain inside the ST and NT specimens before the hydrogen pre-charging process. If the hydrogen accumulation during the hydrogen pre-charging process had a great influence on the change in fracture initiation toughness with H_D, the macroscopic fracture stresses in the slow strain

rate tensile tests of the ST and NT specimens should decrease gradually with increasing H_D. As shown in **Figure 4**, however, the macroscopic fracture stresses of the ST and NT specimens also decreased significantly for the small values of H_D. Consequently, we can propose that the rapid decrease of fracture initiation toughness with small H_D, confirmed in **Figure 7 (a)**, is an intrinsic characteristic of hydrogen-related intergranular fracture, and cannot be accounted from the pre-accumulation of hydrogen around the fatigue pre-crack during the hydrogen pre-charging process.

As shown in **Figure 4**, the macroscopic fracture stresses in the slow strain rate tensile tests of the ST and NT specimens decreased suddenly with small H_D, and further increasing of H_D did not change the macroscopic fracture stresses very much. Because this tendency is similar to the change in fracture initiation toughness with H_D (**Figure 7 (a)**), we can say that the stage for start of crack propagation contributed very much to the macroscopic fracture stress in the slow strain rate tensile test.

Figures 6 (b) and 7 (b) demonstrated that the tearing modulus, corresponding to crack-growth resistance, decreased rather gradually with increasing H_D. Consequently, the increase of H_D affected the crack propagation stage more than the crack initiation as well as the start of crack propagation stages. We can assume that a certain amount of hydrogen was necessary to accumulate locally around the crack tip for further crack propagation. With increasing H_D (global H_D), necessary stress level to induce the hydrogen accumulation decreased, resulting in the decrease of crack-growth resistance. The decrease of crack-growth resistance led to the macroscopic continuous crack propagation, that was observed in the SEM / SE images of **Figure 9**. Though the fracture properties (fracture initiation

toughness and tearing modulus) were summarized as a function of global H_D as shown in **Figure 7**, it is better to correlate the fracture properties to local hydrogen content at crack initiation site or tip of propagating crack. Because local hydrogen content can be expressed as a function of hydrostatic tensile stress and plastic strain [52-55], finite element simulation can evaluate local hydrogen content. In the next paper, we will discuss the fracture properties quantitatively from the viewpoint of local hydrogen content at fracture site.

One of the important findings in the present paper is that the stable crack propagations were confirmed in the hydrogen-related intergranular fracture of the high strength martensitic steel. To date, stable crack propagations in hydrogen embrittlement have been recognized in austenitic stainless steels [33, 34, 36, 37], ferrite – pearlite steels [31], and tempered Cr-Mo / Ni-Cr-Mo steels [38], whose sensitivities to hydrogen embrittlement are not as high. As shown in **Figure 4**, sensitivity to hydrogen embrittlement of the martensitic steel used in the present study was notably high and hydrogen-charged specimens exhibited premature fracture within the elastic strain regime during the slow strain rate tensile tests. Nevertheless, we found that the hydrogen-related intergranular cracks propagated in a stable manner as shown in the $J - \Delta a$ resistance curves of **Figure 6 (b)**. This leads to an important suggestion that hydrogen-related intergranular fracture essentially involves a stable crack propagation process, even though macroscopic premature fracture occurs. The SEM / SE images of **Figure 9** indicate that the macroscopic crack propagations were rather continuous when H_D was large. As shown in the SEM / BSE image and the EBSD orientation map of **Figures 11 (c, d)**, however, there

were many small un-cracked ligaments on the prior austenite grain boundary and a part of the micro-crack existed slightly away from the prior austenite grain boundary. The microstructure observation results indicate that the hydrogen-related crack propagated in a stepwise manner on a microscopic scale. In addition to crack blunting by plastic deformation and to sub-cracks formation, discontinuous crack propagation would result in stable crack propagation with increment of J-integral. Therefore, we infer that the microscopic discontinuous crack propagation could be the possible reason for the stable crack propagation in the hydrogen-related intergranular fracture.

5. Conclusions

In the present paper, we quantitatively evaluated the mechanical response of hydrogen-related fractures in an as-quenched martensitic steel, and correlated it to the crack propagation behavior analyzed by SEM and EBSD. The following conclusions were reached.

1. The slow strain rate tensile tests revealed that the macroscopic fracture stresses of both the ST and NT specimens decreased suddenly with small concentrations of diffusible hydrogen (H_D around 0.5 wt. ppm) and that a further increase in H_D did not change the fracture stress very much.
2. We found from the $J - \Delta a$ resistance curves that the hydrogen-related cracks propagated in a stable manner even when H_D was large. The fracture initiation toughness decreased significantly for small values of H_D, around 0.5 wt. ppm. With further increasing H_D, however, the fracture

initiation toughness did not change and remained almost constant. On the other hand, the tearing modulus decreased rather gradually with increasing H_D. Accordingly, we can propose that increase of H_D affected crack propagation stage rather than crack initiation as well as start of crack propagation stages.

3. The microstructure observations confirmed that the hydrogen-related macroscopic cracks propagated rather continuously when H_D was large. The macroscopic continuous crack propagation would be originated from the decrease of tearing modulus with increasing H_D. On a microscopic scale, however, we found that there were many small un-cracked ligaments on the prior austenite grain boundary, and a part of the micro-crack existed slightly away from the prior austenite grain boundary. Accordingly, we concluded that the hydrogen-related crack propagated discontinuously in a stepwise manner on a microscopic scale. The microscopic discontinuous crack propagation could be the possible reason for the stable crack propagation.

Acknowledgement

This study was financially supported by JSPS KAKENHI Grant Number JP15H04158 and JP19H02459, the Elements Strategy Initiative for Structural Materials (ESISM) from MEXT Japan and the Innovative Structural Materials Association (ISMA). A.S. would like to acknowledge Prof. Y. Hagihara at Sophia University and Prof. M. Ohata at Osaka University for fruitful discussions.

References

[1] Tetelman AS, Robertson WD. Direct observation and analysis of crack propagation in iron-3% silicon single crystals. Acta Metall 1963;11:415-426.

[2] Petch NJ. The lowering of fracture-stress due to surface adsorption. Philos Mag 1956;1:331-337.

[3] Tromans D. On surface energy and the hydrogen embrittlement of iron and steels. Acta Metall Mater 1994;42:2043-2049.

[4] Lynch SP. Environmentally assisted cracking: Overview of evidence for an adsorption-induced localised-slip process. Acta Metall 1988;36:2639-2661.

[5] Oriani RA, Josephic PH. Equilibrium aspects of hydrogen-induced cracking of steels. Acta Metall 1974;22:1065-1074.

[6] Gerberich WW, Chen YY. Hydrogen-controlled cracking – An approach to threshold stress intensity. Metall Trans A 1975;6A:271-278.

[7] Oriani RA, Josephic PH. Equilibrium and kinetic studies of the hydrogen-assisted cracking of steel. Acta Metall 1977;25:979-988.

[8] Beachem CD. A new model for hydrogen-assisted cracking (Hydrogen "Embrittlement"). Metall Trans 1972;3:437-451.

[9] Birnbaum HK, Sofronis P. Hydrogen-enhanced localized plasticity - a mechanism for hydrogen-related fracture. Mater Sci Eng 1994;A176:191-202.

[10] Ferreira PJ, Robertson IM, Birnbaum HK. Hydrogen effects on the interaction between dislocations. Acta Mater 1998;46:1749-1757.

[11] Robertson IM. The effect of hydrogen on dislocation dynamics. Eng Fract Mech 1999;64:649-673.

[12] Nagumo M. Function of hydrogen in embrittlement of high-strength steels. ISIJ Int 2001;41:590-598.

[13] Nagumo M, Matsuda H. Function of hydrogen in intergranular fracture of martensitic steels. Philos Mag A 2002;82:3415-3425.

[14] Robertson IM, Sofronis P, Nagao A, Martin ML, Wang S, Gross DW, Nygren KE. Hydrogen embrittlement understood. Metall Mater Trans B 2015;46B:1085-1103.

[15] Marder AR, Krauss G. The morphology of martensite in iron-carbon alloys. Trans ASM 1967;60:651-660.

[16] Marder JM, Marder AR. The morphology of iron-nickel massive martensite. Trans ASM 1969;62:1-10.

[17] Kim YH, Morris Jr JW. The nature of quasicleavage fracture in tempered 5.5Ni steel after hydrogen charging. Metall Trans A 1983;14A:1883-1888.

[18] Kim YH, Kim HJ, Morris Jr JW. The influence of precipitated austenite on hydrogen embrittlement in 5.5Ni steel. Metall Mater Trans A 1986;17A:1157-1164.

[19] Nagao A, Smith CD, Dadfarnia M, Sofronis P, Robertson IM. The role of hydrogen in

hydrogen embrittlement fracture of lath martensitic steel. Acta Mater 2012;60:5182-5189.

[20] Shibata A, Takahashi H, Tsuji N. Microstructural and crystallographic features of hydrogen-related crack propagation in low carbon martensitic steel. ISIJ Int 2012;52:208-212.

[21] Shibata A, Murata T, Takahashi H, Matsuoka T, Tsuji N. Characterization of hydrogen-related fracture behavior in as-quenched low-carbon martensitic steel and tempered medium-carbon martensitic steel. Metall Mater Trans A 2015;46A:5685-5696.

[22] Shibata A, Momotani Y, Murata T, Matsuoka T, Tsuboi M, Tsuji N. Microstructural and crystallographic features of hydrogen-related fracture in lath martensitic steels. Mater Sci Technol 2017;33:1524-1532.

[23] Okada K, Shibata A, Takeda Y, Tsuji N. Crystallographic feature of hydrogen-related fracture in 2Mn-0.1C ferritic steel. Int J Hydrogen Energy 2018;43:11298-11306.

[24] Banerji SK, McMahon Jr CJ, Feng HC. Intergranular fracture in 4340-type steels: Effects of impurities and hydrogen. Metall Trans A 1978;9A:237-247.

[25] Craig BD, Krauss G. The structure of tempered martensite and its susceptibility to hydrogen stress cracking. Metall Trans A 1980;11A:1799-1808.

[26] Wang M, Akiyama E, Tsuzaki K. Effect of hydrogen and stress concentration on the notch tensile strength of AISI 4135 steel. Mater Sci Eng A 2005;398:37-46.

[27] Wang M, Akiyama E, Tsuzaki K. Effect of hydrogen on the fracture behavior of high strength steel during slow strain rate test. Corros Sci 2007;49:4081-4097.

[28] Takarasawa K, Ikeda R, Ishikawa N, Ishigaki R. Effects of grain size and dislocation density on the susceptibility to high-pressure hydrogen environment embrittlement of high-strength low-alloy steels. Int J Hydrogen Energy 2012;37:2669-2675.

[29] Shibata A, Matsuoka T, Ueno A, Tsuji N. Fracture surface topography analysis of the hydrogen-related fracture propagation process in martensitic steel. Int J Fract 2017;205:73-82.

[30] Shinohara Y, Madi Y, Besson J. Anisotropic ductile failure of a high-strength line pipe steel. Int J Fract 2016;197:127-145.

[31] Nagumo M, Yoshida H, Shimomura Y, Kadokura T. Ductile crack growth resistance in hydrogen-charged steels. Mater Trans 2001;42:132-137.

[32] Scheider I, Pfuff M, Dietzel W. Simulation of hydrogen assisted stress corrosion cracking using the cohesive model. Eng Fract Mech 2008;75:4283-4291.

[33] Somerday BP, Dadfarnia M, Balch DK, Nibur KA, Cadden CH, Sofronis P. Hydrogen-assisted crack propagation in austenitic stainless steel fusion welds. Metall Mater Trans A 2009;40A:2350-2362.

[34] Nibur KA, Somerday BP, Balch DK, San Marchi C. The role of localized deformation in hydrogen-assisted crack propagation in 21Cr-6Ni-9Mn stainless steel. Acta Mater 2009;57:3795-3809.

[35] Falkenberg R, Brocks W, Dietzel W, Scheider I. Modelling the effect of hydrogen on ductile

tearing resistance of steels. Int J Mat Res 2010;101:989-996.

[36] Nibur KA, Somerday BP, San Marchi C, Balch DK. Effects of strength and microstructure on hydrogen-assisted crack propagation in 22Cr-13Ni-5Mn stainless steel forgings. Metall Mater Trans A 2010;41A:3348-3357.

[37] Jackson HF, Nibur KA, San Marchi C, Puskar JD, Somerday BP. Hydrogen-assisted crack propagation in 304L/308L and 21Cr–6Ni–9Mn/308L austenitic stainless steel fusion welds. Corros Sci 2012;60:136-144.

[38] Nibur KA, Somerday BP, San Marchi C, Foulk III JW, Dadfarnia M, Sofronis P. The relationship between crack-tip strain and subcritical cracking thresholds for steels in high-pressure hydrogen gas. Metall Mater Trans A 2013;44A:248-269.

[39] Thodla R, Piza Paes MT, Gerst B. Hydrogen assisted cracking of AISI 4137M steel in O&G environments. Int J Hydrogen Energy 2015;40:17051-17064.

[40] Peral LB, Zafra A, Belzunce J, Rodríguez C. Effects of hydrogen on the fracture toughness of CrMo and CrMoV steels quenched and tempered at different temperatures. Int J Hydrogen Energy 2019;44:3953-3965.

[41] Álvarez G, Peral LB, Rodríguez C, García TE, Belzunce FJ. Hydrogen embrittlement of structural steels: effect of the displacement rate on the fracture toughness of high-pressure hydrogen pre-charged samples. Int J Hydrogen Energy 2019;44:15634-15643.

[42] Morito S, Tanaka H, Konishi R, Furuhara T, Maki T. The morphology and crystallography of

lath martensite in Fe-C alloys. Acta Mater 2003;51:1789-1799.

[43] Choo WY, JY Lee. Thermal analysis of trapped hydrogen in pure iron. Metall Mater A 1982;13A:135-140.

[44] Bandyopadhay N, Kameda J, McMahon, Jr CJ. Hydrogen-induced cracking in 4340-type steel: effects of composition, yield strength, and H_2 pressure. Metall Trans 1983;14A:881-888.

[45] Thomas RLS, Scully JR, Gangloff RP. Internal hydrogen embrittlement of ultrahigh-strength AERMET 100 steel. Metall Mater Trans A 2003;34A:327-344.

[46] Kameda J, McMahon, Jr CJ. Solute segregation and hydrogen-induced intergranular fracture in an alloy steel. Metall Trans 1983;14A:903-911.

[47] Chan KS. A new criterion for brittle-to-ductile fracture transition. Acta Metall 1989;37:1217-1226.

[48] Petit T, Ritter G, Besson J, Morgeneyer TF. Impact of machine stiffness on ‘‘pop-in’’ crack propagation instabilities. Eng Fract Mech 2018;202:405-422.

[49] Luppo MI, Ovejero-Garcia J. The influence of microstructure on the trapping and diffusion of hydrogen in a low carbon steel. Corros Sci 1991;32:1125-1136.

[50] Takai K, Seki J, Homma Y. Observation of trapping sites of hydrogen and deuterium in high-strength steels by using secondary ion mass spectrometry. Mater Trans JIM 1995;36:1134-1139.

[51] Momotani Y, Shibata A, Terada D, Tsuji N. Effect of strain rate on hydrogen embrittlement in low-carbon martensitic steel. Int J Hydrogen Energy 2017;42:3371-3379.

[52] Sofronis P, McMeeking RM. Numerical analysis of hydrogen transport near a blunting crack tip. J Mech Phys Solids 1989;37:317-350.

[53] Sofronis P, Liang Y, Aravas N. Hydrogen induced shear localization of the plastic flow in metals and alloys. Eur J Mech A/Solids 2001;20:857-872.

[54] Ahn DC, Sofronis P, Dodds Jr RH. On hydrogen-induced plastic flow localization during void growth and coalescence. Int J Hydrogen Energy 2007;32:3437-3742.

[55] Dadfarnia M, Sofronis P, Neeraj T. Hydrogen interaction with multiple traps: Can it be used to mitigate embrittlement?. Int J Hydrogen Energy 2011;36:10141-10148.

Figure captions

Figure 1 Optical microscopy image of the heat-treated specimen.

Figure 2 Schematic illustrations of the specimen geometries (unit: mm); (a) smooth tensile bar specimen, (b) notched tensile bar specimen with a notch radius of 2.4 mm, (c) compact tension specimen.

Figure 3 Relationship between diffusible hydrogen content and current density in the cathodically pre-hydrogen charging.

Figure 4 (a, b) Nominal stress – nominal strain curves of the ST specimens (a) and the NT specimens (b) with different H_D and (c) changes in macroscopic fracture stress with H_D (open circles: ST specimens, solid circles: NT specimens). The H_D corresponds to average value of each charging condition shown in Figure 3. In the case of the uncharged ST specimen, the maximum nominal flow stress (tensile strength) was plotted in (c).

Figure 5 SEM / SE images showing fracture surfaces after the slow strain rate tensile tests; (a) the uncharged ST specimen, (b) the uncharged NT specimen, (c, e) the hydrogen-charged ST specimen (H_D = 4.00 wt. ppm) and (d, f) the hydrogen-charged NT specimen (H_D = 4.00 wt. ppm). The

positions of typical dimples and quasi-cleavage facets are indicated by white arrows.

Figure 6 (a) Load – crack mouth opening displacement curves and (b) crack-growth resistance curves ($J - \Delta a$ resistance curves) of the CT specimens with different H_D.

Figure 7 Changes in (a) fracture initiation toughness (J_{IC}) and (b) tearing modulus (T_R) with H_D. The H_D corresponds to average value of each charging condition shown in Figure 3

Figure 8 SEM / SE images showing fracture surfaces after the unloading compliance tests; (a) the uncharged CT specimen and (b-d) the hydrogen-charged CT specimens ((b) H_D = 0.28 wt. ppm, (c) H_D = 0.42 wt. ppm, (d) H_D = 4.00 wt. ppm). The positions of typical dimples and quasi-cleavage facets are indicated by white arrows.

Figure 9 SEM / SE images showing mid-thickness sections of the CT specimens after the unloading compliance tests; (a) the uncharged CT specimen and (b-e) the hydrogen-charged CT specimens ((b) H_D = 0.28 wt. ppm, (c) H_D = 0.42 wt. ppm, (d) H_D = 1.01 wt. ppm, (e) H_D = 4.00 wt. ppm). The white arrows indicate the positions of un-cracked ligaments.

Figure 10 (a, c) SEM / BSE images and (b, d) EBSD orientation maps taken at a region ahead of the

main crack in the uncharged CT specimen after the unloading compliance test. The observed area of (c, d) is white rectangle indicated in (a). The black solid lines and white broken lines indicate the positions of micro-cracks and prior austenite grain boundaries, respectively.

Figure 11 (a, c) SEM / BSE images and (b, d) EBSD orientation maps taken at a region ahead of the main crack in the hydrogen-charged CT specimen (H_D = 4.00 wt. ppm) after the unloading compliance test. The observed area of (c, d) is white rectangle indicated in (a). The black solid lines, white broken lines, red arrow and yellow arrows indicate the positions of micro-cracks, prior austenite grain boundaries, micro-cracks deviated from the prior austenite grain boundary and small un-cracked ligaments, respectively.

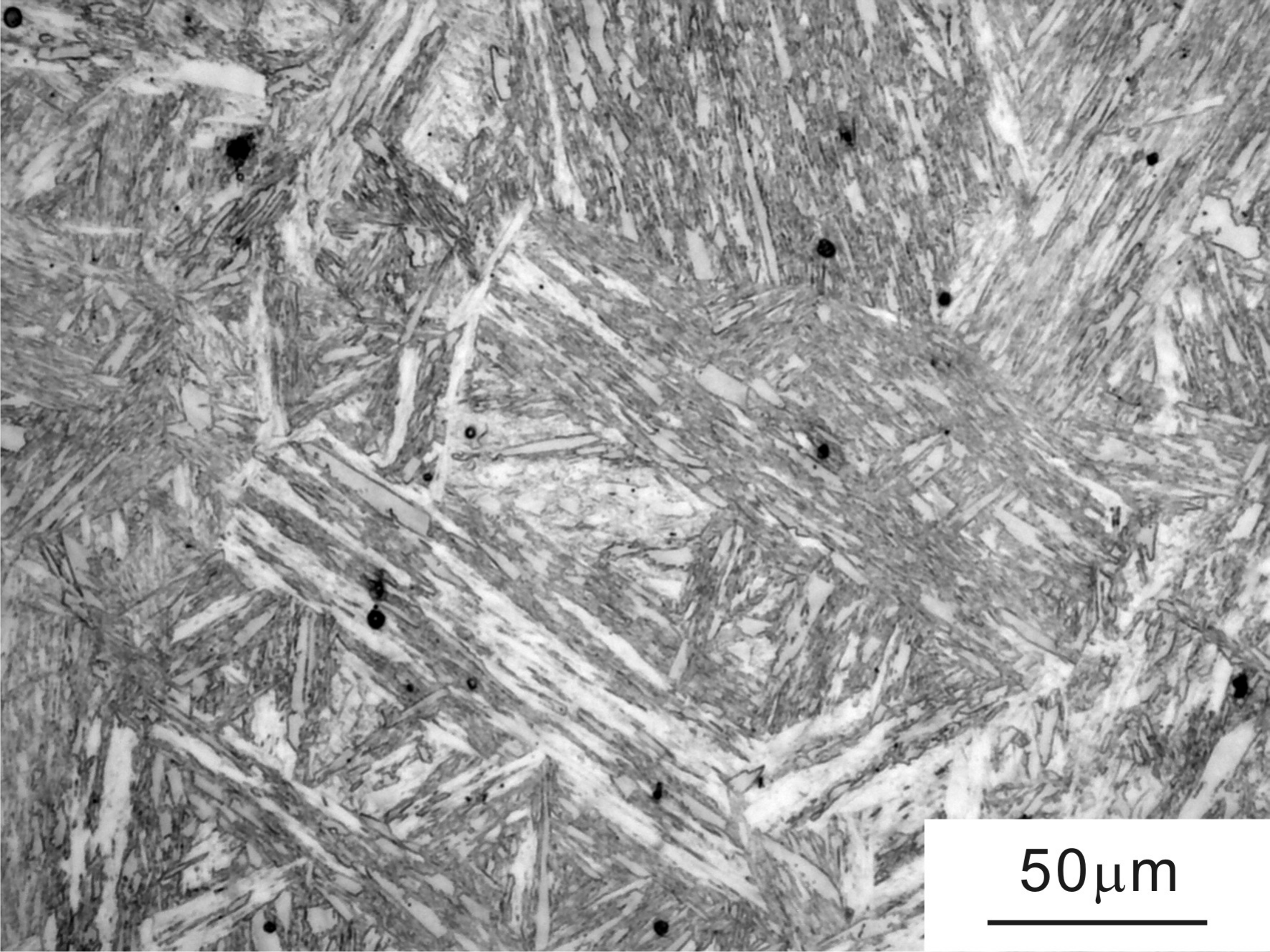
50μm

(a)

ST specimen

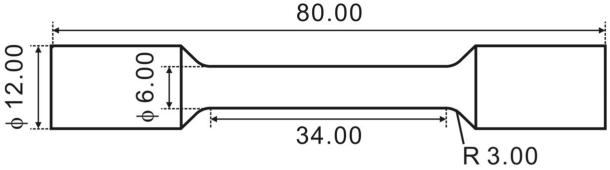

unit: [mm]

(b)

NT specimen

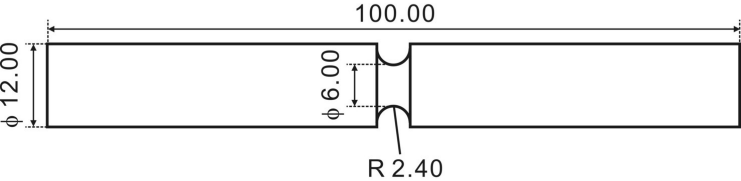

(c)

CT specimen

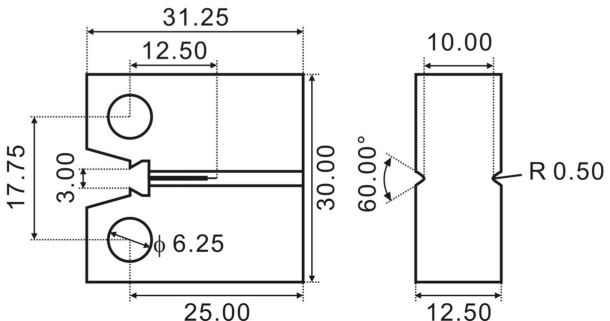

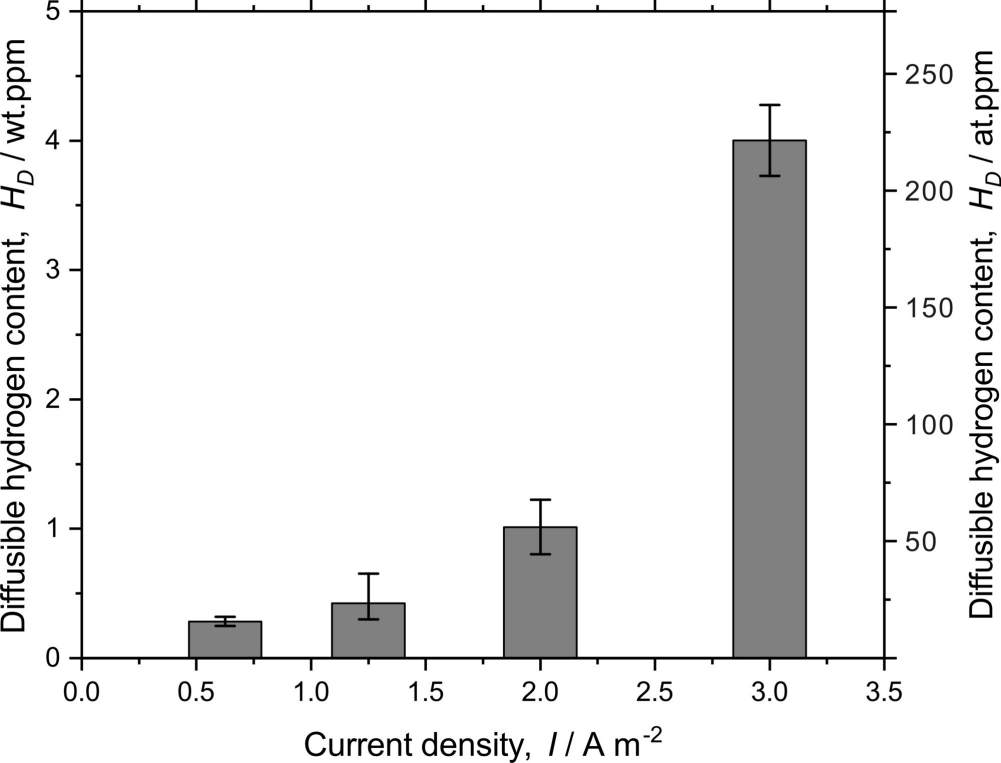
Diffusible hydrogen content, H_D / wt.ppm
Diffusible hydrogen content, H_D / at.ppm
Current density, I / A m^{-2}
0
1
2
3
4
5
50
100
150
200
250
0.0
0.5
1.0
1.5
2.0
2.5
3.0
3.5

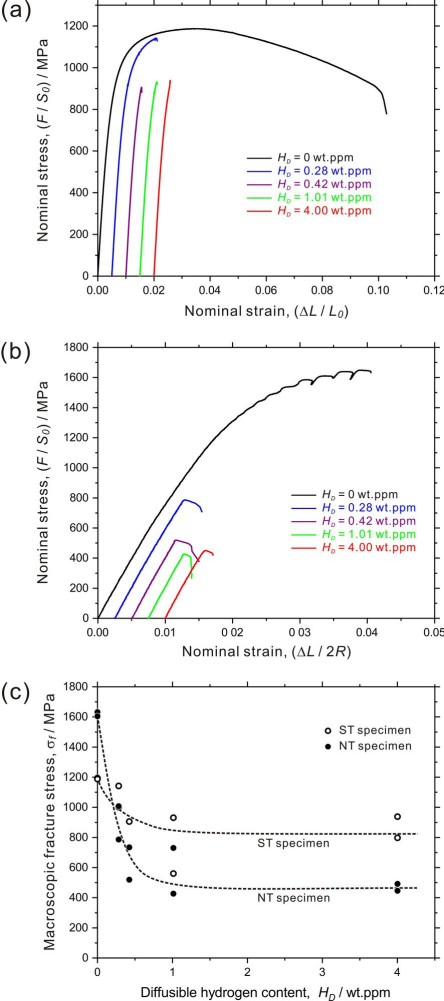
(a)
Nominal stress, (F / S_0) / MPa
Nominal strain, $(\Delta L / L_0)$
H_D = 0 wt.ppm
H_D = 0.28 wt.ppm
H_D = 0.42 wt.ppm
H_D = 1.01 wt.ppm
H_D = 4.00 wt.ppm
(b)
Nominal stress, (F / S_0) / MPa
Nominal strain, $(\Delta L / 2R)$
H_D = 0 wt.ppm
H_D = 0.28 wt.ppm
H_D = 0.42 wt.ppm
H_D = 1.01 wt.ppm
H_D = 4.00 wt.ppm
(c)
Macroscopic fracture stress, σ_f / MPa
Diffusible hydrogen content, H_D / wt.ppm
ST specimen
NT specimen
ST specimen
NT specimen

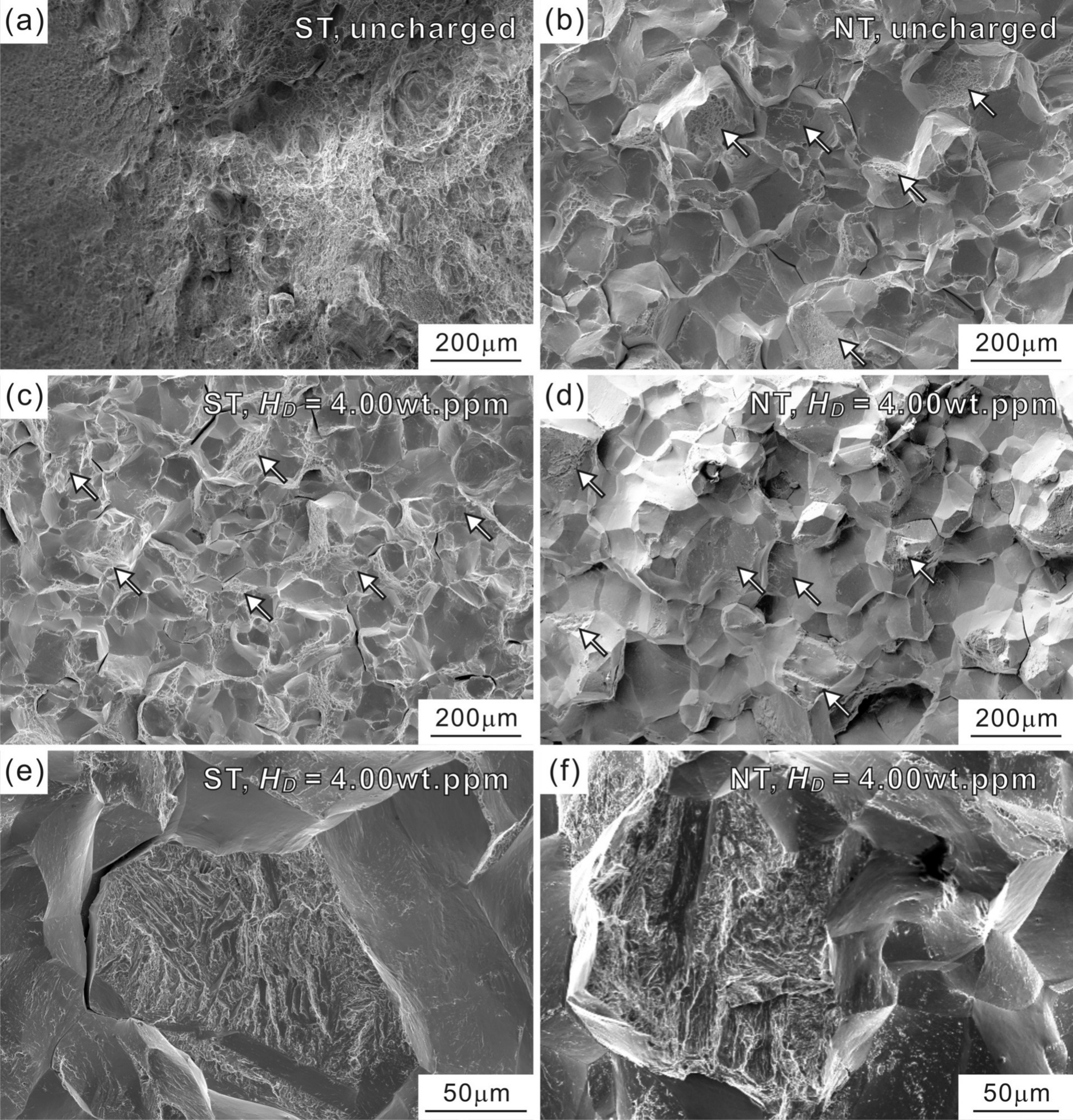
(a)
ST, uncharged
200μm
(b)
NT, uncharged
200μm
(c)
ST, H_D = 4.00wt.ppm
200μm
(d)
NT, H_D = 4.00wt.ppm
200μm
(e)
ST, H_D = 4.00wt.ppm
50μm
(f)
NT, H_D = 4.00wt.ppm
50μm

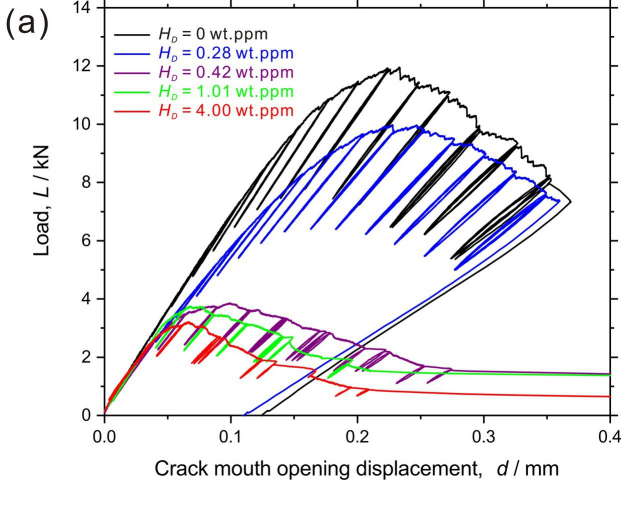
(a)
H_D = 0 wt.ppm
H_D = 0.28 wt.ppm
H_D = 0.42 wt.ppm
H_D = 1.01 wt.ppm
H_D = 4.00 wt.ppm
Load, L / kN
Crack mouth opening displacement, d / mm
0
2
4
6
8
10
12
14
0.0
0.1
0.2
0.3
0.4

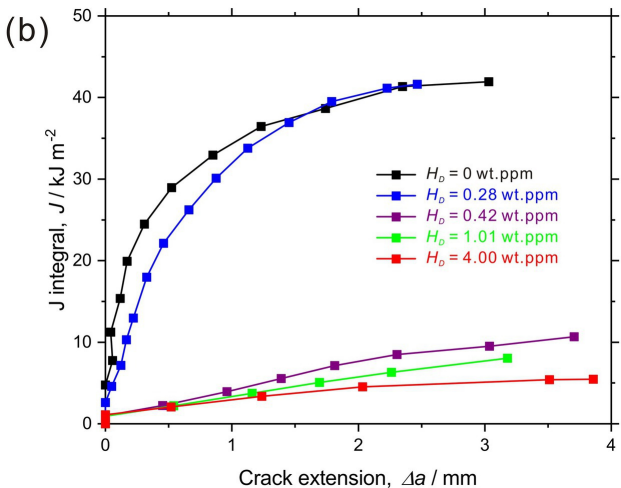
(b)
H_D = 0 wt.ppm
H_D = 0.28 wt.ppm
H_D = 0.42 wt.ppm
H_D = 1.01 wt.ppm
H_D = 4.00 wt.ppm
J integral, J / kJ m^{-2}
Crack extension, Δa / mm
0
10
20
30
40
50
0
1
2
3
4

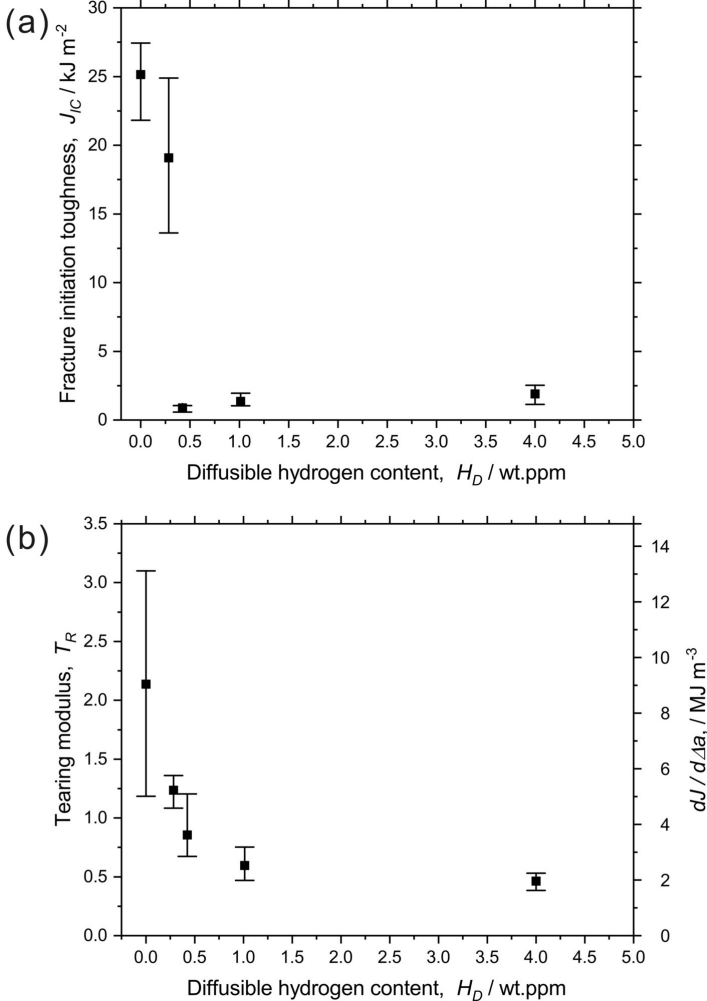
(a)
Fracture initiation toughness, J_{IC} / kJ m^{-2}
0
5
10
15
20
25
30
0.0
0.5
1.0
1.5
2.0
2.5
3.0
3.5
4.0
4.5
5.0
Diffusible hydrogen content, H_D / wt.ppm
(b)
Tearing modulus, T_R
$dJ / d\Delta a$, / MJ m^{-3}
0.0
0.5
1.0
1.5
2.0
2.5
3.0
3.5
0
2
4
6
8
10
12
14
Diffusible hydrogen content, H_D / wt.ppm

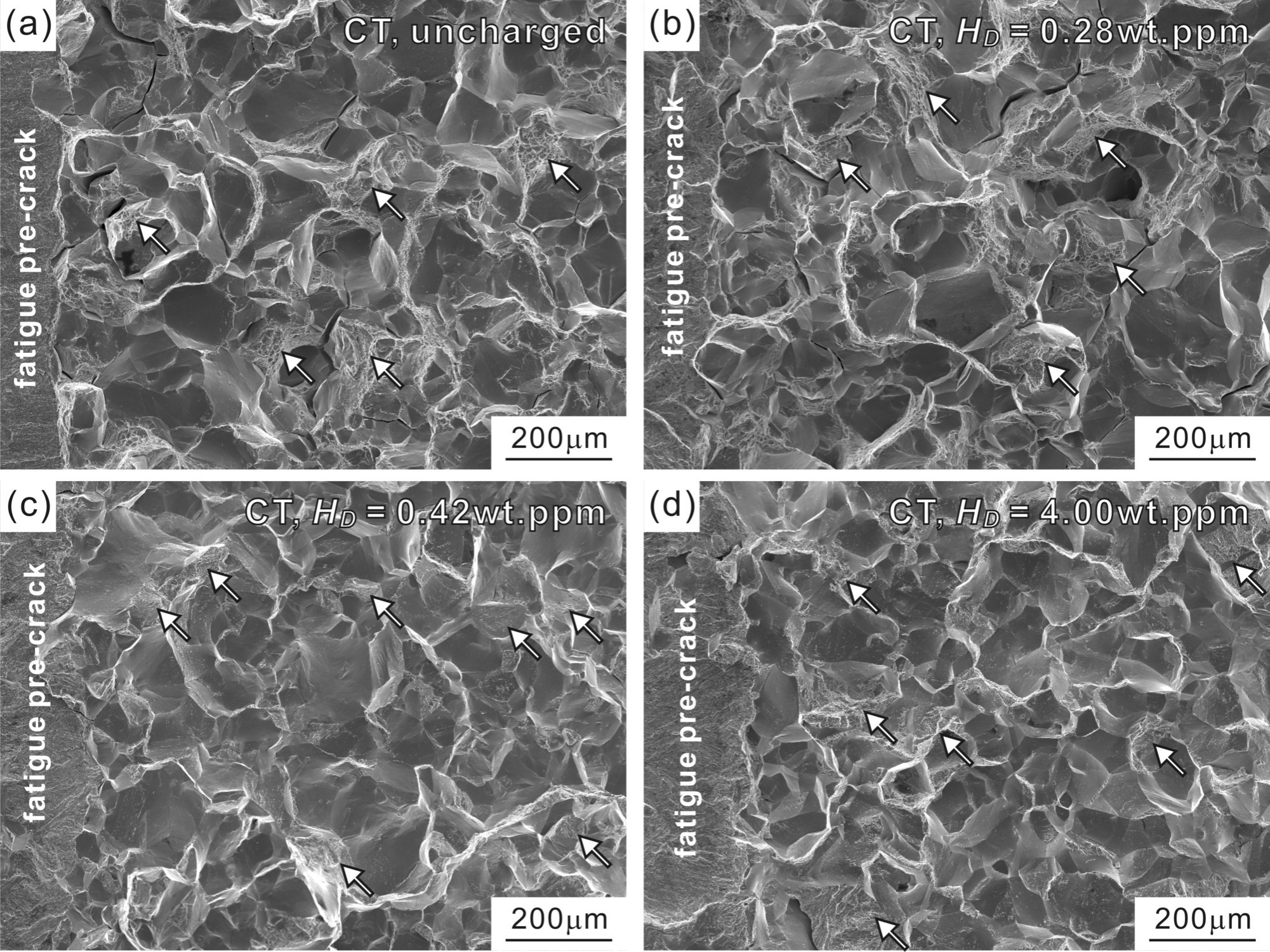
(a)
CT, uncharged
fatigue pre-crack
200μm
(b)
CT, H_D = 0.28wt.ppm
fatigue pre-crack
200μm
(c)
CT, H_D = 0.42wt.ppm
fatigue pre-crack
200μm
(d)
CT, H_D = 4.00wt.ppm
fatigue pre-crack
200μm

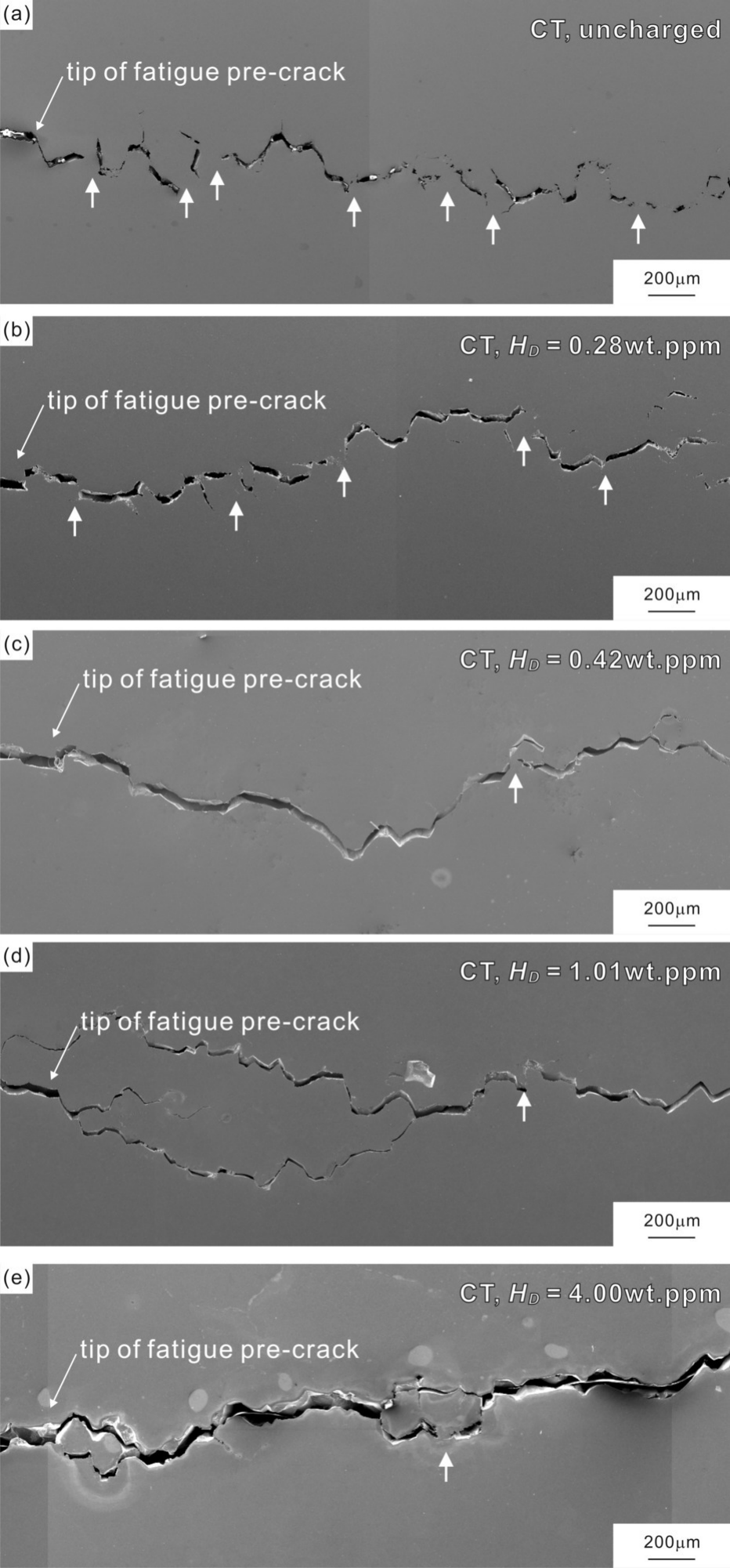
(a)
CT, uncharged
tip of fatigue pre-crack
200μm
(b)
CT, H_D = 0.28wt.ppm
tip of fatigue pre-crack
200μm
(c)
CT, H_D = 0.42wt.ppm
tip of fatigue pre-crack
200μm
(d)
CT, H_D = 1.01wt.ppm
tip of fatigue pre-crack
200μm
(e)
CT, H_D = 4.00wt.ppm
tip of fatigue pre-crack
200μm

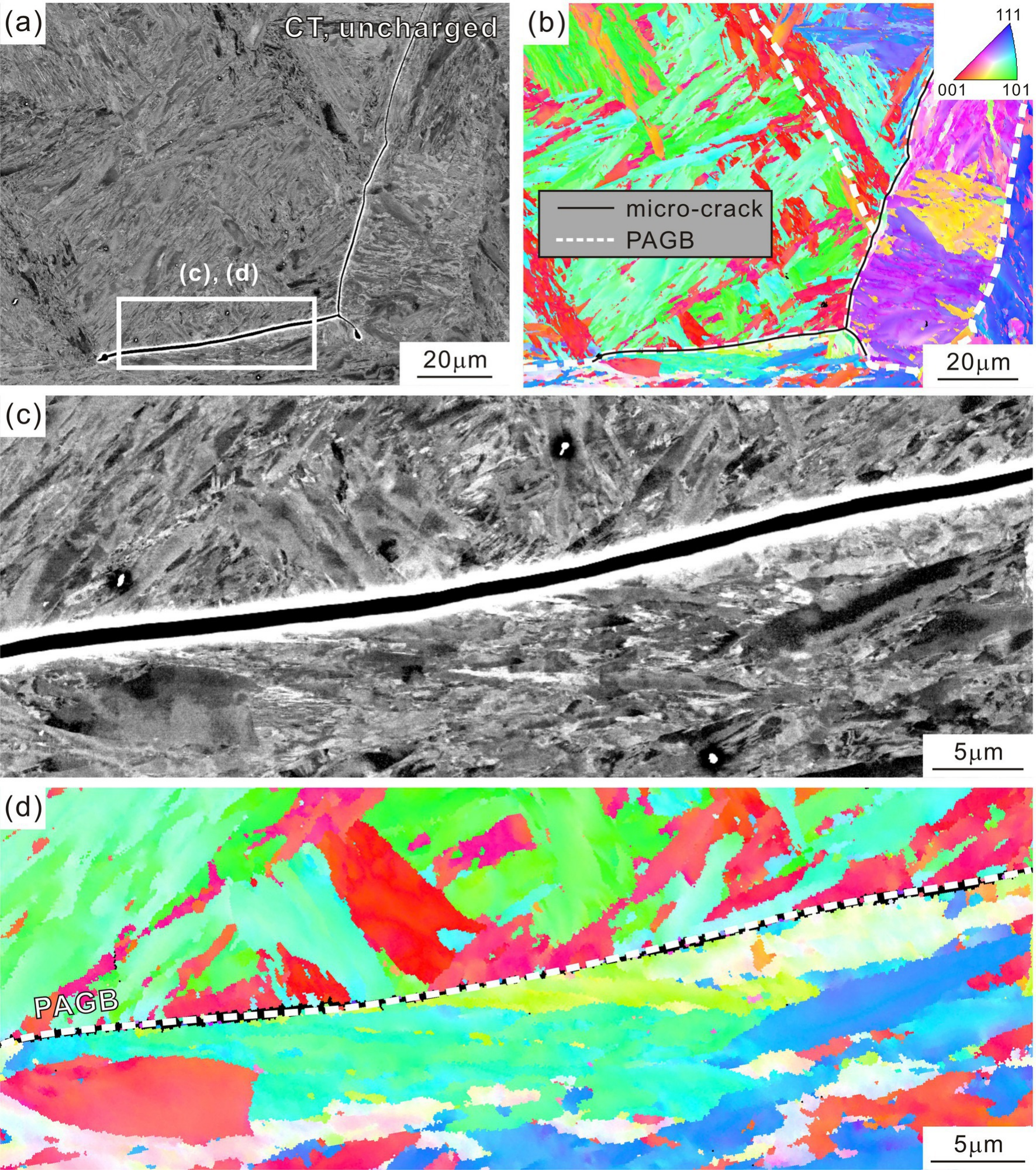
(a)
CT, uncharged
(c), (d)
20μm
(b)
111
001
101
micro-crack
PAGB
20μm
(c)
5μm
(d)
PAGB
5μm

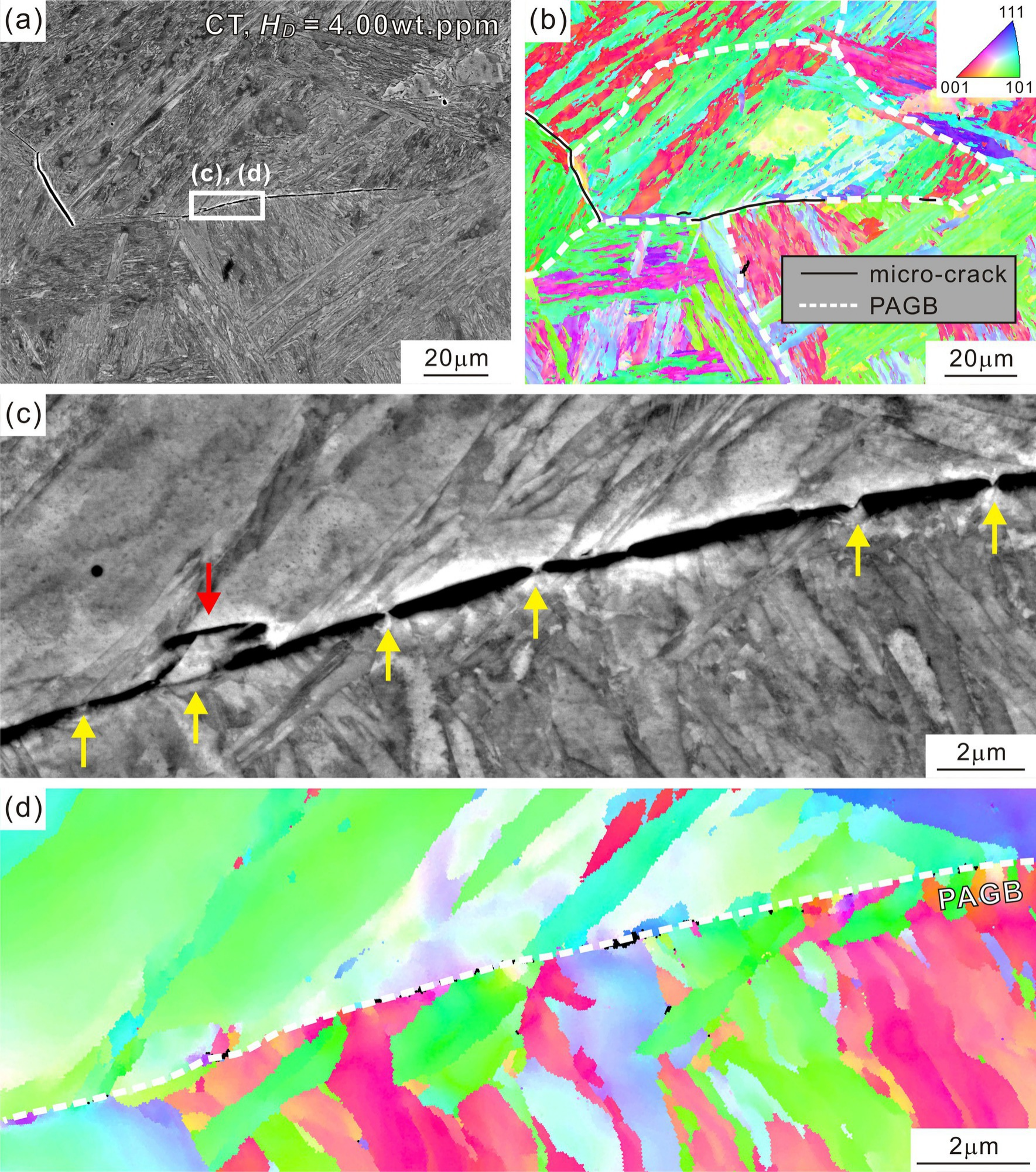
(a)
CT, H_D = 4.00wt.ppm
(c), (d)
20μm
(b)
111
001
101
micro-crack
PAGB
20μm
(c)
2μm
(d)
PAGB
2μm

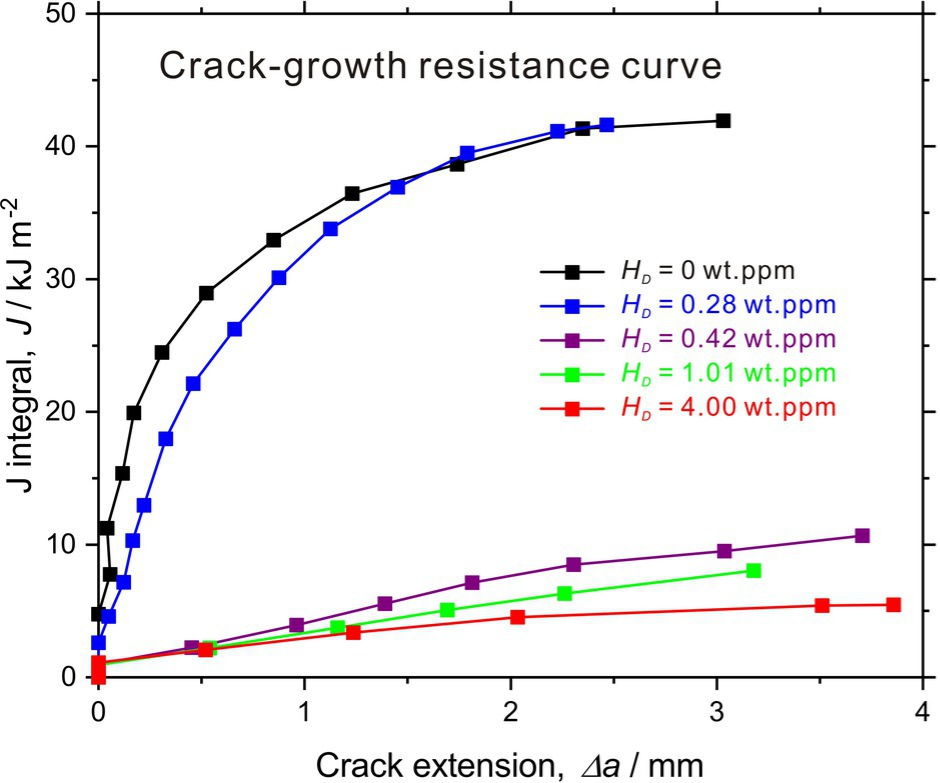
Crack-growth resistance curve
J integral, J / kJ m-2
Crack extension, Δa / mm
H_D = 0 wt.ppm
H_D = 0.28 wt.ppm
H_D = 0.42 wt.ppm
H_D = 1.01 wt.ppm
H_D = 4.00 wt.ppm
0
10
20
30
40
50
0
1
2
3
4

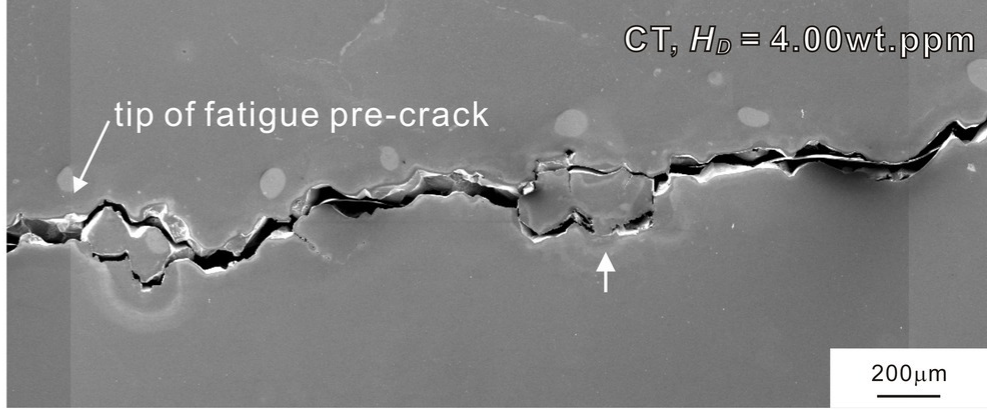
CT, H_D = 4.00wt.ppm
tip of fatigue pre-crack
200μm

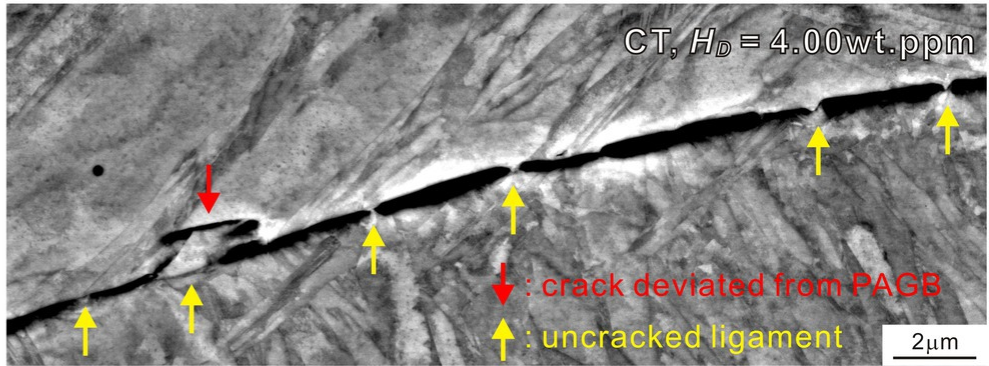
CT, H_D = 4.00wt.ppm
: crack deviated from PAGB
: uncracked ligament
2μm